Article

A Novel Coherent Integration Algorithm for Maneuvering Target Detection Based on Symmetric Instantaneous Autocorrelation Function

Yunpeng Mi [1,2], Yunhua Zhang [1,2,*] and Jiefang Yang [1,2]

[1] CAS Key Laboratory of Microwave Remote Sensing, National Space Science Center, Chinese Academy of Sciences, Beijing 100190, China; biyunpeng16@mails.ucas.ac.cn (Y.M.); yangjiefang@mirslab.cn (J.Y.)
[2] University of Chinese Academy of Sciences, Beijing 100049, China
* Correspondence: zhangyunhua@mirslab.cn

Abstract: Detection and parameter estimation of maneuvering targets having a jerking motion are some of the challenging problems for modern radar systems. Such targets usually introduce range migration (RM) and Doppler frequency migration (DFM) problems leading to serious performance degradation in detection. To address these problems, a novel coherent integration (CI) algorithm is proposed based on a new symmetric instantaneous autocorrelation function (NSIAF), which can be utilized to reduce the order on the slow time and to eliminate the linear range migration (LRM) first. Then, the jerk and acceleration of the target are estimated after applying the keystone transform (KT) and the scaled Fourier transform (SFT); both of these are then used to construct the reference function for matched filtering. Finally, CI and target detection can be accomplished by the scaled inverse Fourier transform (SCIFT) after matched filtering. Both simulation data (this work) and practical radar experiment data (data set of others) were processed to validate the proposed algorithm. Compared with other representative algorithms, our algorithm can achieve a good balance between computational complexity and detection performance.

Keywords: coherent integration (CI); maneuvering target detection; motion parameter estimation; new symmetric instantaneous autocorrelation function (NSIAF)

1. Introduction

The method and algorithm for coherent integration (CI) of echoes from highly maneuvering targets (MaTs), along with motion parameter estimation, have been attracting growing attention, and significant efforts have made in research as part of the rapid development of modern radars [1–5]. Due to the feasible low-radar cross-section of maneuvering targets, the returned radar signal can be quite weak, which can make the detection more difficult. With the help of long-time CI techniques, the MaT detection performance of radar can be significantly improved [6–9]. However, target maneuvering can cause high-order range migration (RM) and Doppler frequency migration (DFM), which creates considerable challenges for CI.

In order to address the linear range migration (LRM) caused by the target velocity, several algorithms have been developed, e.g., the keystone transform (KT) can correct the LRM without requiring knowledge about the target's velocity beforehand [10,11]. However, its performance might be limited due to velocity ambiguity resulting from the resampling process. Additionally, the interpolation operation can also affect the detection performance while resulting in a significant computational burden. The Radon–Fourier transform (RFT) can remove the LRM and realize CI by jointly searching in the target's motion parameter space. The axis-rotation moving-target detection (AR-MTD) [12] corrects the range migration (RM) by rotating the fast-time and slow-time axes at the same time and completes the CI by moving target detection (MTD). Both the RFT and the AR-MTD

suffer from heavy computational burdens because of motion parameter searching. The scaled inverse Fourier transform (SCIFT) [13] can eliminate the LRM and accomplish the CI without any searching procedure. However, the aforementioned algorithms cannot deal with a target experiencing acceleration or a jerking motion.

The acceleration of MaTs will induce quadratic range migration (QRM) and linear Doppler frequency migration (LDFM). The Radon-fractional Fourier transform (RFRFT) [14] was proposed to deal with MaTs experiencing acceleration. The RFRFT can extract the target trajectory and eliminate the LDFM by applying the Radon transform and the fractional Fourier transform together. Nonetheless, the RFRFT is hindered by high computational cost resulting from the three-dimensional searching. The second-order KT (SOKT) [15], and the KT-Lv's distribution (KT-LVD) [16] algorithms were developed to reduce the dimension of parameter searching. However, these algorithms still require one-dimensional searching. The discrete polynomial-phase transform (DPT) [17], although it can achieve fast CI without any searching, is not suitable for low signal-to-noise-ratio (SNR) scenarios due to the cross-correlation applied. Additionally, all the above algorithms fail to deal with a maneuvering target experiencing a jerking motion because cubic range migration (CRM) and quadratic Doppler frequency migration (QDFM) are induced.

Although the generalized Radon–Fourier transform (GRFT) [18] is an effective algorithm to accomplish CI regarding acceleration, the brute-force searching of motion parameters significantly increases the computation complexity. In addition, the blind speed side lobe (BSSL) effect may appear due to discrete pulse sampling, finite range resolution, and limited integration time, leading to serious false alarms and CI degradation. The adjacent cross-correlation function (ACCF) applied iteratively [19] is an efficient CI algorithm for MaTs, but the detection performance is sacrificed since the multiple nonlinear operations are conducted with a fixed lag time. The multiple nonlinear operations using variable lag time were studied in [20], demonstrating higher anti-noise performance than the ACCF-based algorithms. Unfortunately, this algorithm is not suitable for maneuvering targets with a jerking motion.

In this paper, we proposed a novel fast CI algorithm for the detection of MaTs with a jerking motion. We first define a new symmetric instantaneous autocorrelation function (NSIAF) with variable lag time, which can be applied to reduce the order on the slow time and eliminate the LRM. Afterwards, the KT and the scaled Fourier transform (SFT) [21] are applied to decouple the range frequency, lag time, and slow time, and obtain the acceleration and jerk estimations, according to which the matched function is constructed and applied. The CI can then be accomplished using SCIFT [13], and in the final step, the target is detected through peak searching. The proposed algorithm can be implemented with a low computational cost by circumventing parameter searching. Comparisons with other representative algorithms indicate that this proposed algorithm can achieve a favorable balance between the computational complexity and the detection performance. Finally, both simulated data and practical radar data are processed to demonstrate the effectiveness of the proposed algorithm.

The remainder of this paper is organized as follows. Section 2 provides a brief introduction to the signal model. In Section 3, the proposed algorithm is described in detail. In Section 4, both simulated and practical radar data are processed to validate the proposed algorithm. Finally, the conclusion is drawn in Section 5.

2. Signal Model

Suppose that a pulse-Doppler radar transmits a linear frequency modulation (LFM) signal as

$$s(t, t_n) = \text{rect}\left(\frac{t}{T_p}\right) \exp(j2\pi f_c t + j\pi K t^2) \tag{1}$$

where $\text{rect}(\cdot)$ denotes a rectangle function with pulse duration of T_p, $K = B/T_p$ is the frequency modulation rate, B is the signal bandwidth, f_c is the carrier frequency, and t denotes the fast time.

In this work, we focus on a maneuvering target with a jerking motion, so the instantaneous distance of the target relative to the radar can be expressed as [6,7,22]

$$R(t_n) = R_0 + v t_n + \frac{a t_n^2}{2} + \frac{b t_n^3}{6} \tag{2}$$

where $t_n = n T_r$ $(n = 1, 2, \cdots, N)$ is the slow time, N and T_r are respectively the pulse number and the pulse repetition interval, R_0, v, a, and b denote the initial radial range, radial velocity, radial acceleration, and radial jerk.

The received echo signal after down conversion can be expressed as

$$s_r(t, t_n) = A_0 \text{rect}\left[\frac{t - 2R(t_n)/c}{T_p}\right] \exp\left[j\pi K \left(t - \frac{2R(t_n)}{c}\right)^2\right] \exp\left[-j\frac{4\pi R(t_n)}{\lambda}\right] \tag{3}$$

where A_0 is the complex amplitude, c is the light speed, f_c is the carrier frequency of the transmitted signal, and $\lambda = c/f_c$ is the wavelength.

The signal after pulse compression can be expressed as

$$\begin{aligned}
s_c(t, t_n) &= A_1 \text{sin c}\left[B\left(t - \frac{2(R_0 + v t_n + a t_n^2/2 + b t_n^3/6)}{c}\right)\right] \\
&\times \exp\left(-j4\pi \frac{R_0 + v t_n + a t_n^2/2 + b t_n^3/6}{\lambda}\right)
\end{aligned} \tag{4}$$

where A_1 denotes the signal amplitude after pulse compression and $\text{sinc}(x) = \sin(\pi x)/\pi x$ denotes the SINC function.

As one can see from (4), the peak position and the phase of the range compressed signal are time varied with slow time t_n. Once the position variation exceeds the range resolution $\rho_r = c/2B$ in the SINC function, the compressed echo will be situated at cells having different ranges, i.e., the terms t_n, $t_n{}^2$, and $t_n{}^3$ induce LRM, QRM, and CRM, respectively.

From the exponential term in (4), the instantaneous Doppler frequency can be derived as

$$\begin{aligned}
f_d(t_n) &= \frac{2}{\lambda} \frac{d(R_0 + v t_n + a t_n^2/2 + b t_n^3/6)}{d t_n} \\
&= \frac{2v}{\lambda} + \frac{2a t_n}{\lambda} + \frac{b t_n^2}{\lambda}
\end{aligned} \tag{5}$$

As clearly shown in (5), the Doppler frequency varies with the slow time t_n due to the radial acceleration a and jerk b, which respectively induce the LDFM and QDFM.

The LRM, QRM, CRM, LDFM, and QDFM all can lead to serious CI loss and should be corrected to achieve good performance in MaT detection.

3. Novel Coherent Integration Algorithm for Maneuvering Target Detection
3.1. Principle of the Proposed Algorithm

As we know, the result of (4) is obtained by performing inverse fast Fourier transform (IFFT) on the following signal with respect to the range frequency f_r:

$$\begin{aligned}
S_c(f_r, t_n) &= A_2 \text{rect}\left(\frac{f_r}{B}\right) \exp\left[-j4\pi(f_r + f_c)\frac{R_0}{c}\right] \\
&\times \exp\left[-j4\pi(f_r + f_c)\frac{v t_n + a t_n^2/2 + b t_n^3/6}{c}\right]
\end{aligned} \tag{6}$$

where A_2 denotes the signal amplitude after FFT.

In the following, the NSIAF is defined with variable lag time regarding $S_c(f_r, t_n)$ in the (f_r, t_n) domain as

$$\begin{aligned}
R(f_r, t_n, \tau) &= S\left(f_r, t_n + \tfrac{\tau}{2} + \tau_0\right) S\left(f_r, t_n - \tfrac{\tau}{2} - \tau_0\right) \\
&\times \left[S\left(f_r, t_n + \tfrac{\tau}{2} - \tau_0\right) S\left(f_r, t_n - \tfrac{\tau}{2} + \tau_0\right)\right]^*
\end{aligned} \tag{7}$$

where "$*$" denotes the complex conjugation operation, and τ and τ_0 are the variable lag time and a constant time delay, respectively. Here τ_0 is set as $0.089 T_c$ [23,24], $T_c = N T_r$ is the total integration time.

By substituting (6) into (7), we obtain

$$R(f_r, t_n, \tau) = A_3 \exp\left[-j8\pi \frac{f_r + f_c}{c} \tau_0 \tau(a + bt_n)\right] \tag{8}$$

where $A_3 = A_2^4 \text{rect}(f_r/B)$ is the signal amplitude of NSIAF.

Equation (8) shows the LRM has been eliminated and the highest order of the term t_n has been reduced from three to one. However, the coupling between f_r, τ, and t_n still exists, which can be decoupled by the KT [10,11], via variable substitution as follows:

$$(f_c + f_r)\tau = f_c \tau_n \tag{9}$$

where τ_n is the new lag-time variable.

Then, the signal becomes

$$R_{KT}(f_r, t_n, \tau_n) = A_3 \exp\left[-j8\pi \frac{f_c}{c} \tau_n \tau_0 (a + bt_n)\right] \exp(j2\pi f_r \cdot 0) \tag{10}$$

As (10) shows, f_r has been decoupled from τ and t_n, and the echo energies of pulses are all distributed along the f_r axis [15], which can be accumulated directly via summation:

$$\begin{aligned} Q(t_n, \tau_n) &= \text{SUM}_{f_r}[R_{KT}(f_r, t_n, \tau_n)] \\ &= A_4 \exp\left(-j8\pi \frac{f_c}{c} a\tau_n \tau_0\right) \exp\left(-j8\pi \frac{f_c}{c} b\tau_n \tau_0 t_n\right) \end{aligned} \tag{11}$$

where $\text{SUM}_{f_r}[\cdot]$ denotes the addition operation along the f_r axis, and A_4 is the signal amplitude after the addition operation.

In the following, we decouple τ_n and t_n by conducting SFT on (11) as follows:

$$\begin{aligned} Q(f_n, \tau_n) &= \text{SFT}_{t_n}[Q(t_n, \tau_n)] \\ &= \int_{t_n} Q(t_n, \tau_n) \exp[-j2\pi \tau_n f_n t_n] dt_n \\ &= A_5 \exp\left(-j8\pi \frac{f_c}{c} \tau_n \tau_0 a\right) \delta\left(f_n + \frac{4}{\lambda} \tau_0 b\right) \end{aligned} \tag{12}$$

where A_5 denotes the signal amplitude after SFT, f_n is the scaled frequency variable corresponding to t_n, and $\text{SFT}_{t_n}[\cdot]$ denotes the SFT operation with respect to t_n.

One can see from (12) that t_n has been decoupled from τ_n. By applying the FFT on (12) with respect to τ_n, we have

$$Q(f_n, f_{\tau_n}) = A_6 \delta\left(f_n + \frac{4}{\lambda} \tau_0 b\right) \delta\left(f_{\tau_n} + \frac{4}{\lambda} \tau_0 a\right) \tag{13}$$

where f_{τ_n} is the frequency variable corresponding to τ_n, and A_6 denotes the signal amplitude after FFT.

According to (13), the acceleration a and the jerk b can be estimated by searching for the peak position of $(-4a\tau_0/\lambda, -4b\tau_0/\lambda)$ in the $f_n - f_{\tau_n}$ domain, as

$$\begin{cases} \hat{a} = -\frac{\lambda \hat{f}_{\tau_n}}{4\tau_0} \\ \hat{b} = -\frac{\lambda \hat{f}_n}{4\tau_0} \end{cases} \tag{14}$$

where $\hat{f}_n$ and $\hat{f}_{\tau_n}$ are the peak values along the f_n and f_{τ_n} axes, respectively, and $\hat{a}$ and $\hat{b}$ are the estimated a and b, respectively.

Based on (14), we can construct the corresponding matched function used to compensate for the acceleration and jerk as follows:

$$H_c(f_r, t_n) = \exp\left[j4\pi(f_r + f_c)\frac{\hat{a}t_n^2/2 + \hat{b}t_n^3/6}{c}\right] \tag{15}$$

By multiplying (6) with (15), we get

$$
\begin{aligned}
S_1(f_r, t_n) & = S_c(f_r, t_n) H_c(f_r, t_n) \\
& = A_2 \mathrm{rect}\left(\frac{f_r}{B}\right) \exp\left[-j4\pi(f_r + f_c)\frac{vt_n}{c}\right]
\end{aligned}
\tag{16}
$$

As shown in (16) the QRM, LDFM, and QDFM have all been eliminated; LRM has not been eliminated, but can be easily eliminated by SCIFT [13]. So, the final CI result can be achieved:

$$
\begin{aligned}
S_2(f_r, f_d) & = \mathrm{SCIFT}[S_1(f_r, t_n)] \\
& = A_7 \mathrm{sinc}\left[B\left(t - \frac{2R_0}{c}\right)\right]\delta\left(f_d + \frac{2v}{\lambda}\right)
\end{aligned}
\tag{17}
$$

where SCIFT[·] denotes the SCIFT operation.

The whole flowchart of the proposed algorithm is given in Figure 1, which is explained in detail as follows:

Step 1: Perform the pulse compression and range FFT to obtain $S_c(f_r, t_n)$ in (6).

Step 2: Calculate the NSIAF based on (7), and denote the result as $R(f_r, t_n, \tau)$.

Step 3: Conduct KT on $R(f_r, t_n, \tau)$, followed by the addition operation along the f_r axis to get $Q(t_n, \tau_n)$.

Step 4: Apply the SFT and FFT on $Q(t_n, \tau_n)$ and estimate the acceleration $\hat{a}$ and the jerk $\hat{b}$ through searching the peak position.

Step 5: Construct the matched function based on (15) and multiply it with $S_c(f_r, t_n)$ to get $S_1(f_r, t_n)$.

Step 6: Perform the SCIFT on $S_1(f_r, t_n)$ to realize coherent integration.

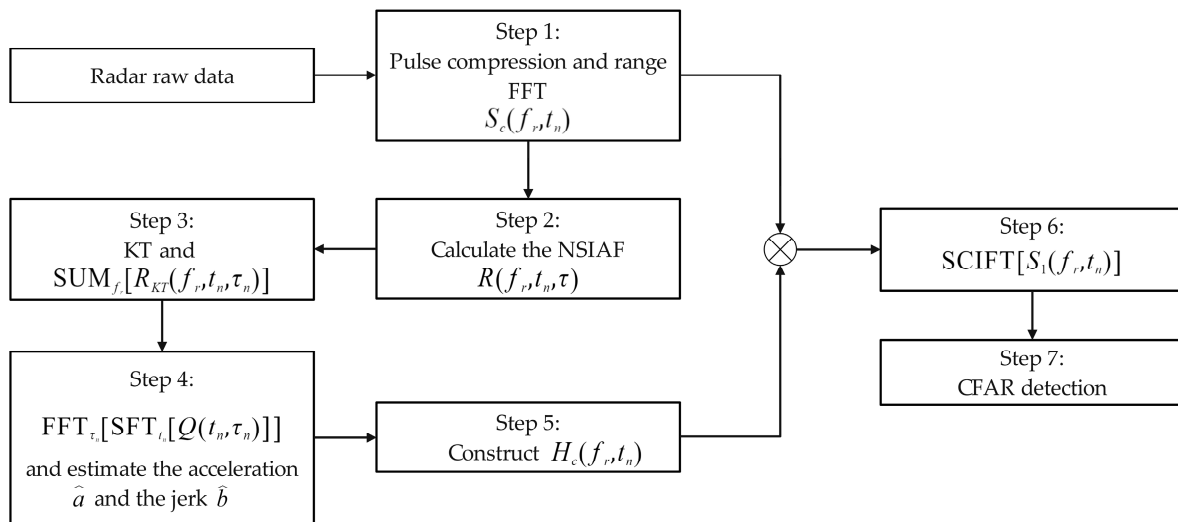Step 7: Carry out the constant false alarm (CFAR) detection to accomplish target detection.

Figure 1. Flowchart of the proposed algorithm.

3.2. Cross-Term Analysis

The above analysis is valid only for a single target scenario. Cross-terms can appear when multiple targets are considered, and these shall be analyzed in the following.

Similar to (6), the received signal backscattered from *K* targets after pulse compression in the range frequency domain can be expressed as

$$
\begin{aligned}
S_c(f_r, t_n) & = \sum_{k=1}^{K} A_{2k} \mathrm{rect}\left(\frac{f_r}{B}\right) \exp\left[-j4\pi(f_r + f_c)\frac{R_0}{c}\right] \\
& \times \exp\left(-j4\pi(f_r + f_c)\frac{v_k t_n + a_k t_n^2/2 + b_k t_n^3/6}{c}\right)
\end{aligned}
\tag{18}
$$

By performing NSIAF on (18), we obtain

$$
\begin{aligned}
R(f_r, t_n, \tau) \quad &= \underbrace{\sum_{k=1}^{K} A_{3k} \exp\left[-j8\pi \frac{f_r + f_c}{c} \tau_0 \tau (a_k + b_k t_n)\right]}_{\mathrm{self-term}} \\
&+ \sum_{i=1}^{K-1} \sum_{j=i+1}^{K} R_{\mathrm{cross},i,j}(f_r, t_n, \tau)
\end{aligned}
\tag{19}
$$

where $R_{\mathrm{cross},i,j}(f_r, t_n, \tau)$ denotes the cross term generated by the *i*th and *j*th target.

After the KT of (9) and addition operation of (11) applied to (19), we obtain

$$
\begin{aligned}
Q(t_n, \tau_n) \quad &= \underbrace{\sum_{k=1}^{K} A_{4k} \exp\left(-j8\pi \frac{f_c}{c} a_k \tau_n \tau_0\right) \exp\left(-j8\pi \frac{f_c}{c} b_k \tau_n \tau_0 t_n\right)}_{\mathrm{self-term}} \\
&+ \sum_{i=1}^{K-1} \sum_{j=i+1}^{K} Q_{\mathrm{cross},i,j}(t_n, \tau_n)
\end{aligned}
\tag{20}
$$

where $Q_{\mathrm{cross},i,j}(t_n, \tau_n)$ is the outcome of $R_{\mathrm{cross},i,j}(f_r, t_n, \tau)$ after KT and addition operations.

After performing SFT and FFT on (20) with respect to t_n and τ_n, respectively, we have

$$
\begin{aligned}
Q(f_n, f_{\tau_n}) \quad &= \sum_{k=1}^{K} A_{6k} \delta\left(f_n + \tfrac{4}{\lambda} \tau_0 b_k\right) \delta\left(f_{\tau_n} + \tfrac{4}{\lambda} \tau_0 a_k\right) \\
&+ \sum_{i=1}^{K-1} \sum_{j=i+1}^{K} Q_{\mathrm{cross},i,j}(f_n, f_{\tau_n})
\end{aligned}
\tag{21}
$$

where $Q_{\mathrm{cross},i,j}(f_n, f_{\tau_n})$ denotes the cross-term of $Q(f_n, f_{\tau_n})$. The detailed expressions of $R_{\mathrm{cross},i,j}(f_r, t_n, \tau)$, $Q_{\mathrm{cross},i,j}(t_n, \tau_n)$, and $Q_{\mathrm{cross},i,j}(f_n, f_{\tau_n})$ can be found in Appendix A.

As (21) shows, all the *K* maneuvering targets can be well focused in the $f_n - f_{\tau_n}$ domain, whose peak locations correspond to $(-4a_k\tau_0/\lambda, -4b_k\tau_0/\lambda)$, while, as shown in Appendix A, the cross-terms are dispersed in the $f_n - f_{\tau_n}$ domain, so the cross-terms' energies are much smaller than those of the self-terms.

Additionally, we should point out that the proposed algorithm may suffer from performance degradation in scenarios when both stronger and weaker maneuvering targets exist since the cross-terms associated with the strong targets may submerge the self-terms of the weak targets. In this case, the "CLEAN" technique [25] can be adopted to adaptively remove the influence of strong target.

3.3. SNR Loss of the NSIAF

It was pointed out in [22,26–28] that the use of autocorrelation functions will result in SNR loss due to the emergence of additional noise terms. In this subsection, we quantitatively analyze the SNR loss of the NSIAF defined by (7). For the convenience of analysis, we assume the input signal of the NSIAF is included with independent white Gaussian noise. Let

$$
\begin{cases}
S_1 = S\left(f_r, t_n + \frac{\tau}{2} + \tau_0\right), S_2 = S\left(f_r, t_n - \frac{\tau}{2} - \tau_0\right) \\
S_3 = S\left(f_r, t_n + \frac{\tau}{2} - \tau_0\right), S_4 = S\left(f_r, t_n - \frac{\tau}{2} + \tau_0\right) \\
n_1 = n\left(t_n + \frac{\tau}{2} + \tau_0\right), n_2 = n\left(t_n - \frac{\tau}{2} - \tau_0\right) \\
n_3 = n\left(t_n + \frac{\tau}{2} - \tau_0\right), n_4 = n\left(t_n - \frac{\tau}{2} + \tau_0\right)
\end{cases}
\tag{22}
$$

where n_1, n_2, n_3, and n_4 are the Gaussian white noise with variance of σ^2. We define the input SNR as $\mathrm{SNR}_{\mathrm{in}} = A_2^2/\sigma^2$. Substituting (22) into (7) yields

$$
\begin{aligned}
R_n(f_r, t_n, \tau) \quad &= (S_1 + n_1)(S_2 + n_2)[(S_3 + n_3)(S_4 + n_4)]^* \\
&= R_{ns}(f_r, t_n, \tau) + R_{nc}(f_r, t_n, \tau)
\end{aligned}
\tag{23}
$$

where

$$R_{ns}(f_r, t_n, \tau) = A_2^4 \exp\left[-j8\pi \frac{f_r + f_c}{c} \tau_0 \tau (a + b t_n)\right] \tag{24}$$

$$
\begin{aligned}
R_{nc}(f_r, t_n, \tau) \;=\;& n_1 n_2 n_3^* n_4^* + n_1 n_2 n_3^* S_4^* + n_1 n_2 S_3^* n_4^* + n_1 S_2 n_3^* n_4^* + S_1 n_2 n_3^* n_4^* \\
& + n_1 n_2 S_3^* S_4^* + n_1 S_2 n_3^* S_4^* + n_1 S_2 S_3^* n_4^* + S_1 n_2 n_3^* S_4^* + S_1 n_2 S_3^* n_4^* \\
& + S_1 S_2 n_3^* n_4^* + S_1 S_2 S_3^* n_4^* + n_1 S_2 S_3^* S_4^* + S_1 n_2 S_3^* S_4^* + S_1 S_2 n_3^* S_4^*
\end{aligned}
\tag{25}
$$

According to (24) and (25), we can derive

$$E\left[|R_{ns}(f_r, t_n, \tau)|^2\right] = A_2^8 \tag{26}$$

$$E\left[|R_{nc}(f_r, t_n, \tau)|^2\right] = \sigma^8 + 4A_2^2\sigma^6 + 6A_2^4\sigma^4 + 4A_2^6\sigma^2 \tag{27}$$

Thus, the output SNR of the NSIAF is

$$
\begin{aligned}
\mathrm{SNR_{out}} \;=\;& \frac{E\left[|R_{ns}(f_r, t_n, \tau)|^2\right]}{E\left[|R_{nc}(f_r, t_n, \tau)|^2\right]} \\
=\;& \frac{A_2^8}{\sigma^8 + 4A_2^2\sigma^6 + 6A_2^4\sigma^4 + 4A_2^6\sigma^2}
\end{aligned}
\tag{28}
$$

Then the SNR loss can be calculated by

$$\frac{\mathrm{SNR_{out}}}{\mathrm{SNR_{in}}} = \frac{1}{4 + \frac{1}{\mathrm{SNR_{in}^3}} + 4\frac{1}{\mathrm{SNR_{in}^2}} + 6\frac{1}{\mathrm{SNR_{in}}}} \tag{29}$$

As shown in (29), when $\mathrm{SNR_{in}} \gg 1$, $\mathrm{SNR_{out}}/\mathrm{SNR_{in}} \approx 1/4$, the maximum loss of the output SNR is about 6 dB [17].

4. Simulations and Experiments

In this subsection, we evaluate the performance of the proposed algorithm via simulations for both single target and multiple targets. The simulated radar parameters are listed in Table 1.

Table 1. Radar parameters.

Parameters	Value
Carrier frequency	1 GHz
Bandwidth	30 MHz
Sampling frequency	60 MHz
Pulse duration	5 μs
Pulse repetition frequency	400 Hz
Pulse number	500

4.1. Simulation Results for Single MaT

In this simulation, let us consider a MaT whose motion parameters are set as follows: the initial range $R_0 = 150$ km, the radial velocity $v = 480$ m/s, the radial acceleration $a = -35$ m/s^2, and the jerk $b = 16$ m/s^3. This experiment is conducted without considering any noise for the purpose of better revealing the properties of the proposed algorithm. The simulation results are presented in Figure 2.

Figure 2a shows the pulse compression result, where serious RM is shown. Figure 2b presents the $t_n - \tau$ distribution at $f_r = 30$ MHz, i.e., $R(30 \text{ MHz}, t_n, \tau)$. After performing SFT on (11) with respect to t_n, we obtain the result of $Q(f_n, \tau_n)$, as shown in Figure 2c. After performing FFT on $Q(f_n, \tau_n)$ with respect to τ_n, one peak appears, as shown in Figure 2d, according to which the radial acceleration and jerk can be estimated as $\hat{a} = -35.02$ m/s^2 and $\hat{b} = 16.04$ m/s^3, respectively. The final CI by SCIFT is presented in Figure 2e. Obviously, both a and b have been very accurately estimated.
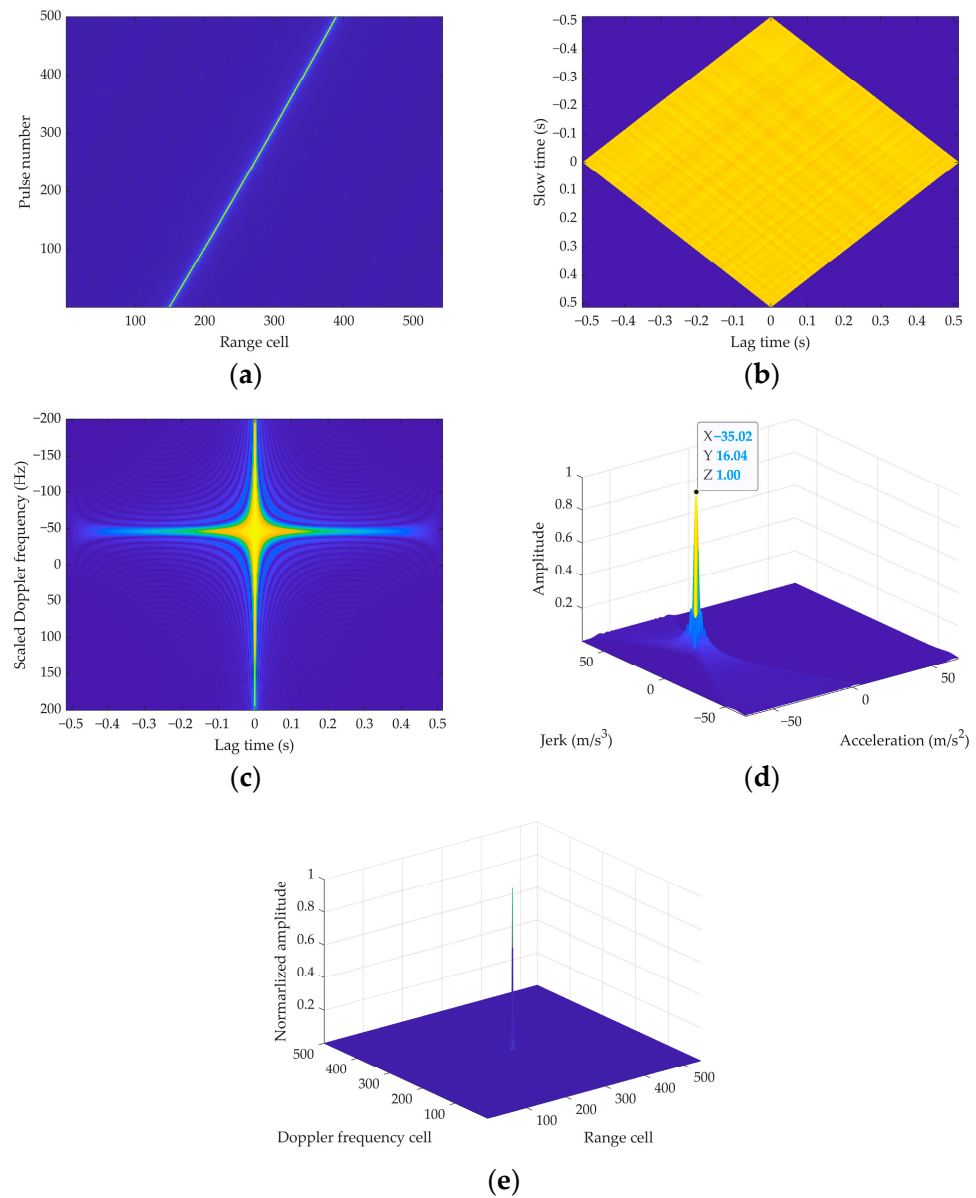
Figure 2. Simulation results for a single target without noise considered. (**a**) Pulse compression. (**b**) NSIAF at $f_r = 30$ MHz. (**c**) $Q(f_n, \tau_n)$. (**d**) $Q(f_n, f_{\tau_n})$. (**e**) CI.

4.2. Simulation Results for Multiple MaTs

We now evaluate the performance of the proposed algorithm on detection of four MaTs with noise considered, whose motion parameters are all different and are listed in Table 2. The echoes are added with complex additive Gaussian white noise, and the different SNRs of the four targets' raw echoes are also listed in Table 2. Figure 3a shows the pulse compression result; as can be seen, four targets are presented with different trajectories. Figure 3b,c present the results of $R(30 \text{ MHz}, t_n, \tau)$ and $Q(f_n, \tau_n)$, respectively. Figure 3d shows the result of $Q(f_n, f_{\tau_n})$, from which one can see four apparent peaks. All the targets can be identified simultaneously even if their amplitudes are different due to different input SNRs. According to (14), the radial accelerations and jerks of the four targets can be estimated, and they are listed in Table 3. According to (15)–(17), the final CI result of the proposed algorithm is given in Figure 3e. The result of iterative ACCF is given in Figure 3f, where the echo energies are all defocused. Figure 3g shows the result of GRFT, where although four peaks corresponding to these four targets can still be located, the BSSLs indicated by the red circle can also result in false targets, besides lowering the detection

probability of the truth target. The MTD [29] result is presented in Figure 3h, where the echo energies are distributed in several range cells and in several Doppler frequency cells, as well due to serious RM and DFM.
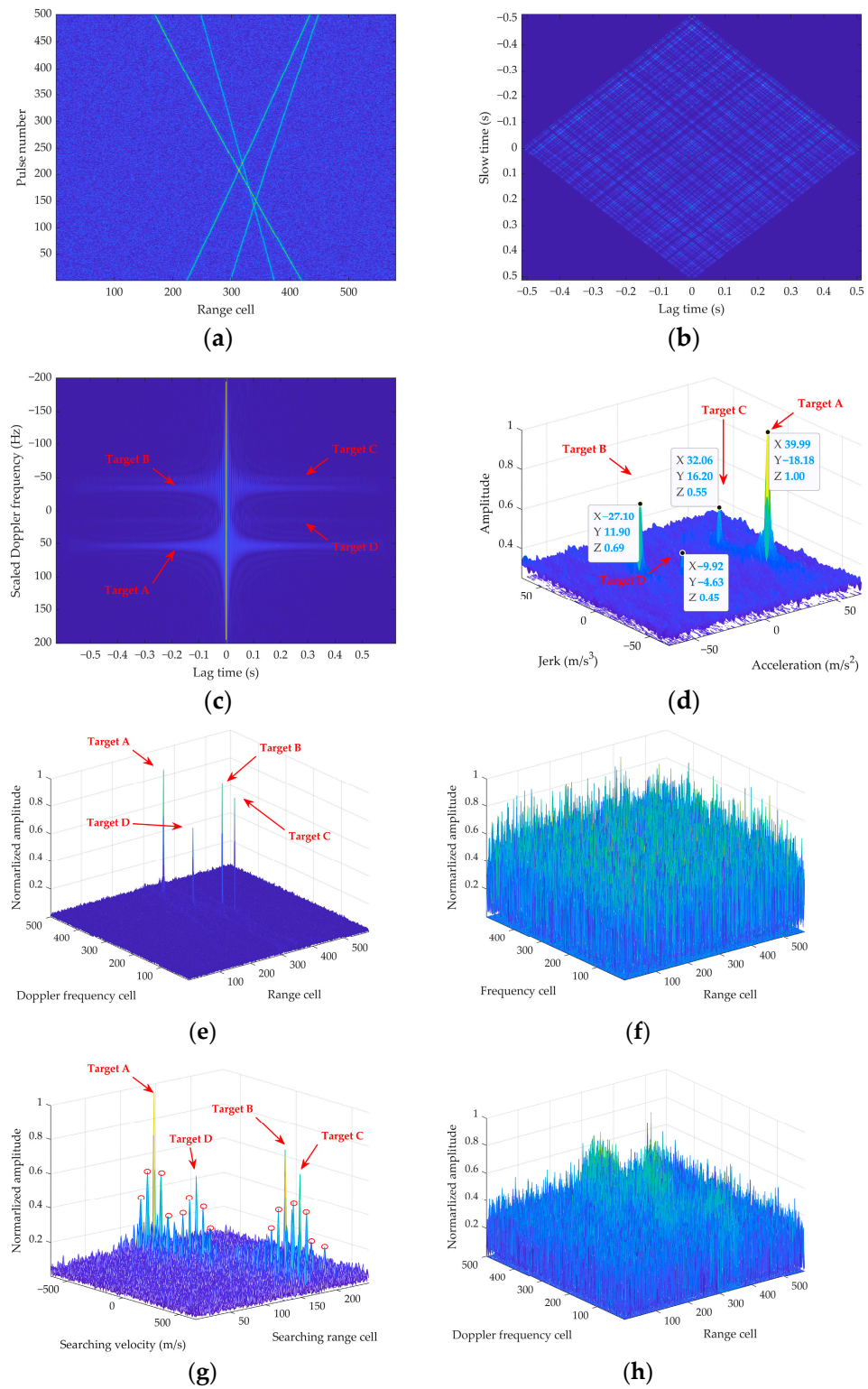

Figure 3. Simulation results for four targets with noise considered. (**a**) Pulse compression. (**b**) NSIAF at $f_r = 30$ MHz. (**c**) $Q(f_n, \tau_n)$. (**d**) $Q(f_n, f_{\tau_n})$. (**e**) CI by our algorithm. (**f**) CI by ACCF iteratively. (**g**) CI by GRFT. (**h**) MTD.

Table 2. Simulated targets' parameters.

Parameters	Target A	Target B	Target C	Target D
SNR (dB)	−11.61	−12.43	−13.85	−14.94
Initial range (km)	150	150.1	150.2	150.05
Radial velocity (m/s)	−500	420	300	−250
Radial acceleration (m/s^2)	40	−27	32	−10
Radial jerk (m/s^3)	−18	12	16	−5

Table 3. Estimated targets' accelerations and jerks.

Estimated Parameters	Target A	Target B	Target C	Target D
Estimated radial acceleration (m/s^2)	39.99	−27.10	32.06	−9.92
Estimated radial jerk (m/s^3)	−18.18	11.90	16.20	−4.63

4.3. Computational Complexity and Detection Performance

In this subsection, the computation complexity and the detection performance of the proposed are compared with that of GRFT and iterative ACCF.

Suppose the numbers of range bins and pulses are M and N, respectively. The computational complexity for the main procedures of the proposed algorithm is composed of four parts, i.e., calculation of $R(f_r, t_n, \tau)$ $[O(MN^2)]$, the operation of Chirp-z-based KT $[O(MN^2 \log N)]$, the FFT and SFT operations $[O(2MN \log N)]$, and the SCIFT $[O(MN^2)]$. Thus, the overall computation complexity of the proposed algorithm is $O(2MN^2 + MN^2 \log N + 2MN \log N)$. For the computational complexities of GRFT and iterative ACCF, one can refer to [18,19], and these are not repeated here. All complexities are listed in Table 4, where N_v, N_a and N_b represent the searching numbers of radial velocity, acceleration, and jerk, respectively, in GRFT. Obviously, if N_v, N_a, and N_b are greater than N (in fact, this is usually the case, especially when accurate estimates are required), the computational burden of our algorithm can be significantly lower than that of GRFT. Although the iterative ACCF algorithm has the lowest computational complexity, its anti-noise performance is inferior to ours, as shall be shown later.

Table 4. Computational complexity.

Algorithms	Computational Complexity
GRFT	$O(N_v N_a N_b MN)$
Iterative ACCF	$O(MN \log N + MN \log M)$
The proposed algorithm	$O(2MN^2 + MN^2 \log N + 2MN \log N)$

In the following, we evaluate the detection performances of the proposed algorithm via Monte Carlo trials. The radar system parameters are the same as those in Table 1, and the target in Section 4.1 is selected. Complex additive white Gaussian noises are added to make the SNRs before pulse compression as [−35:1:0] dB, and 100 Monte Carlo trials are conducted for each SNR value. The detection performances of our algorithm along with the GRFT, iterative ACCF, and MTD are presented in Figure 4, all using the cell averaging constant false alarm (CA-CFAR) by setting the false alarm probability as $P_{fa} = 10^{-5}$. As shown, the GRFT performs the best, whereas our algorithm performs better than the MTD and iterative ACCF.
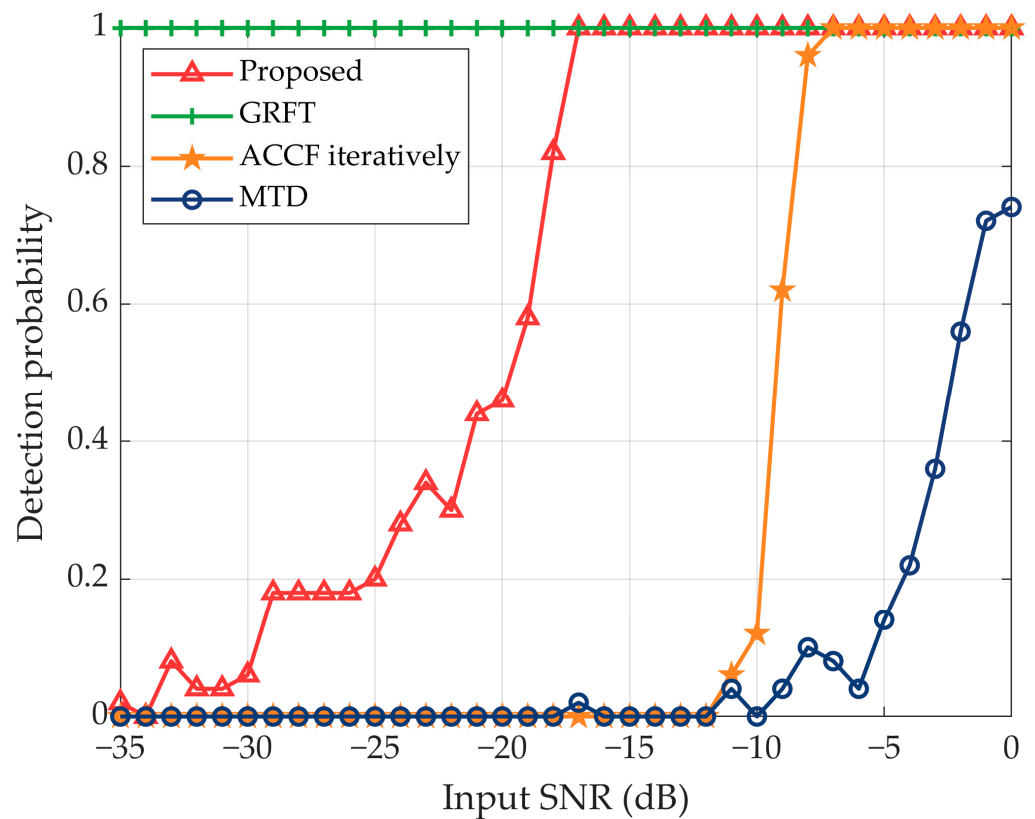
Figure 4. Comparison of detection performances of our algorithm along with the GRFT, iterative ACCF, and MTD.

According to Figure 4 and the above computational complexity analysis, we can conclude that our proposed algorithm can strike a balance between the computational complexity and the detection ability.

4.4. Practical Radar Experiment

In this subsection, the practical Ka-band radar data [30] are processed to validate the proposed algorithm. The basic parameters of the Ka-band radar are provided as follows: the carrier frequency is 35 GHz, the PRF is 32 kHz, and the range cell is about 1.875 m.

The target trajectory is shown in Figure 5a; as can be seen, serious RM exists. Figure 5b shows the MTD result, which shows that the CI performance is degraded due to RM and DFM. The $Q(f_n, f_{\tau_n})$ result is presented in Figure 5c, from which the acceleration and jerk can be estimated as $\hat{a} = 0.31$ m/s^2 and $\hat{b} = 0.99$ m/s^3, respectively, according to the peak position. From the true instant velocities provided by the GPS, the true acceleration and jerk corresponding to the selected data segment can be fitted as $a = 0.26$ m/s^2 and $b = 1.02$ m/s^3, respectively. The true velocity and the fitted curve are presented in Figure 5d, which shows that the estimated a and b are very close to the truth values. Figure 5e shows the final CI result. The Doppler frequency profiles are plotted in Figure 5f; as can be seen, our result is about 7.52 dB better than that of MTD.
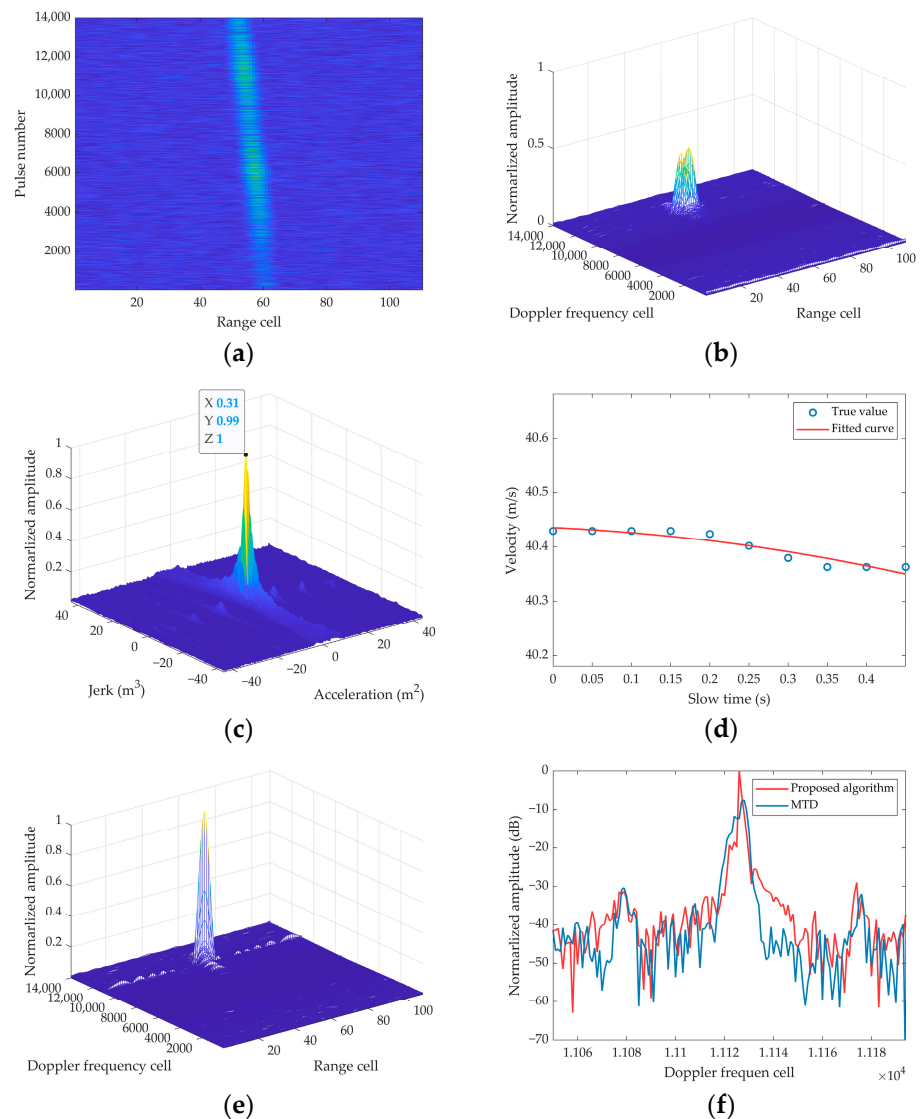
Figure 5. Experimental results on practical radar data. (**a**) Pulse compression. (**b**) MTD. (**c**) $Q(f_n, f_{\tau_n})$ result. (**d**) True value and fitted curve. (**e**) Integrated result. (**f**) Doppler frequency profiles.

5. Conclusions

This paper proposes a novel CI algorithm for MaTs having a jerking motion without the need to search for motion parameters. The NSIAF with variable lag time is defined and used to reduce the order on the slow time and to eliminate the LRM. Then the KT and the SFT are applied to obtain the acceleration and jerk estimations, according to which the matched function is constructed and applied, and the CI and target detection can be finally accomplished using the SCIFT. The searching for motion parameters can be avoided in the whole processes. The performance of the proposed algorithm is compared with that of other representative algorithms, and shows that our algorithm can achieve a good balance between the computational complexity and the detection ability. Processing results of both simulated and practical radar data validate the proposed algorithm very well.

Furthermore, we should point out that the proposed algorithm is not specifically designed for the detection of high- or low-velocity targets. For targets with much lower velocities, the applicability depends on whether the LRM, QRM, CRM, LDFM, and QDFM occur. For some radar systems working at much higher carrier frequencies, the low-speed maneuvering targets can also lead to these problems, in which case our algorithm is still applicable. If this is not the case, i.e., the above migrations do not exist simultaneously,

then some other algorithms with comparatively lower computational complexity can be used to accomplish the coherent integration.

Appendix A

In Appendix A, we discuss the behaviors of the cross-terms in NSIAF processing. The cross-term $R_{\text{cross},i,j}(f_r, t_n, \tau)$ in (19) can be expressed as

$$R_{\text{cross},i,j}(f_r, t_n, \tau) = \sum_{p=1}^{6} R_{\text{cross},i,j,p}(f_r, t_n, \tau) \tag{A1}$$

where

$$
\begin{aligned}
&R_{\text{cross},i,j,1}(f_r, t_n, \tau) \\
&= 2A_{2i}^3 A_{2j} \exp\left\{ j4\pi \frac{f_r+f_c}{c} \left[\begin{array}{c} 3R_{0i} + R_{0j} + (3v_i + v_j)t_n + \frac{1}{2}(a_i - a_j)\tau\tau_0 + \frac{1}{2}(b_i - b_j)\tau\tau_0 t_n \\ + (3a_i + a_j)\left(\frac{1}{2}t_n^2 + \frac{1}{8}\tau^2 + \frac{1}{2}\tau_0^2\right) + (3b_i + b_j)\left(\frac{1}{6}t_n^3 + \frac{1}{8}\tau^2 t_n + \frac{1}{2}\tau_0^2 t_n\right) \end{array} \right] \right\} \\
&\times \cos\left\{ 4\pi \frac{f_r+f_c}{c}\left[(v_i - v_j)\left(\frac{1}{2}\tau - \tau_0\right) + (a_i - a_j)\left(\frac{1}{2}\tau t_n - \tau_0 t_n\right) + (b_i - b_j)\left(\frac{1}{48}\tau^3 - \frac{1}{6}\tau_0^3 + \frac{1}{4}\tau\tau_0^2 - \frac{1}{8}\tau^2\tau_0 + \frac{1}{4}\tau t_n^2 - \frac{1}{2}\tau_0 t_n^2\right)\right] \right\}
\end{aligned}
\tag{A2}
$$

$$
\begin{aligned}
&R_{\text{cross},i,j,2}(f_r, t_n, \tau) \\
&= 2A_{2i}^3 A_{2j} \exp\left\{ j4\pi \frac{f_r+f_c}{c} \left[\begin{array}{c} R_{0i} - R_{0j} + (v_i - v_j)t_n - \frac{1}{2}(3a_i + a_j)\tau\tau_0 - \frac{1}{2}(3b_i + b_j)\tau\tau_0 t_n \\ + (a_i - a_j)\left(\frac{1}{2}t_n^2 + \frac{1}{8}\tau^2 - \frac{1}{2}\tau_0^2\right) + (b_i - b_j)\left(\frac{1}{6}t_n^3 + \frac{1}{8}\tau^2 t_n + \frac{1}{2}\tau_0^2 t_n\right) \end{array} \right] \right\} \\
&\times \cos\left\{ 4\pi \frac{f_r+f_c}{c}\left[(v_i - v_j)\left(\frac{1}{2}\tau + \tau_0\right) + (a_i - a_j)\left(\frac{1}{2}\tau t_n + \tau_0 t_n\right) + (b_i - b_j)\left(\frac{1}{48}\tau^3 + \frac{1}{6}\tau_0^3 + \frac{1}{4}\tau\tau_0^2 + \frac{1}{8}\tau^2\tau_0 + \frac{1}{4}\tau t_n^2 + \frac{1}{2}\tau_0 t_n^2\right)\right] \right\}
\end{aligned}
\tag{A3}
$$

$$
\begin{aligned}
&R_{\text{cross},i,j,3}(f_r, t_n, \tau) \\
&= 2A_{2i}^2 A_{2j}^2 \exp\left\{ -j4\pi \frac{f_r+f_c}{c}\left[\tau\tau_0 t_n (b_i + b_j) + \tau\tau_0(a_i + a_j)\right] \right\} \\
&\times \cos\left\{ 4\pi \frac{f_r+f_c}{c}\left[2(R_{0i} - R_{0j}) + (a_i - a_j)\left(t_n^2 + \frac{1}{4}\tau^2 + \tau_0^2\right) + 2(v_i - v_j)t_n + (b_i - b_j)\left(\frac{1}{3}t_n^3 + \frac{1}{4}\tau^2 t_n + \tau_0^2 t_n\right)\right] \right\}
\end{aligned}
\tag{A4}
$$

$$
\begin{aligned}
&R_{\text{cross},i,j,4}(f_r, t_n, \tau) \\
&= 2A_{2i}^2 A_{2j}^2 \exp\left\{ -j4\pi \frac{f_r+f_c}{c}\left[2\tau\tau_0(a_i + a_j) + 2\tau\tau_0 t_n (b_i + b_j)\right] \right\} \\
&\times \cos\left\{ 4\pi \frac{f_r+f_c}{c}\left[(v_i - v_j)\left(\frac{1}{2}\tau - \tau_0\right) + (a_i - a_j)\left(\frac{1}{2}\tau t_n - \tau_0 t_n\right) + (b_i - b_j)\left(\frac{1}{48}\tau^3 - \frac{1}{6}\tau_0^3 + \frac{1}{4}\tau\tau_0^2 - \frac{1}{8}\tau^2\tau_0 + \frac{1}{4}\tau t_n^2 - \frac{1}{2}\tau_0 t_n^2\right)\right] \right\}
\end{aligned}
\tag{A5}
$$

$R_{\text{cross},i,j,5}(f_r, t_n, \tau)$

$$
= 2A_{2i}A_{2j}^3 \exp\left\{ -j4\pi\frac{f_r+f_c}{c}\left[\begin{array}{c} R_{0i} - R_{0j} - (v_i - v_j)t_n + \frac{1}{2}(a_i + 3a_j)\tau\tau_0 + \frac{1}{2}(b_i + 3b_j)\tau\tau_0 t_n \\ + (a_i - a_j)\left(\frac{1}{2}t_n^2 + \frac{1}{8}\tau^2 + \frac{1}{2}\tau_0^2\right) + (b_i - b_j)\left(\frac{1}{6}t_n^3 + \frac{1}{8}\tau^2 t_n + \frac{1}{2}\tau_0^2 t_n\right) \end{array} \right] \right\}
$$

$$
\times \cos\left\{ 4\pi\frac{f_r+f_c}{c}\left[(v_i - v_j)\left(\frac{1}{2}\tau + \tau_0\right) + (a_i - a_j)\left(\frac{1}{2}\tau t_n + \tau_0 t_n\right) + (b_i - b_j)\left(\frac{1}{48}\tau^3 + \frac{1}{6}\tau_0^3 + \frac{1}{4}\tau\tau_0^2 + \frac{1}{8}\tau^2\tau_0 + \frac{1}{4}\tau t_n^2 + \frac{1}{2}\tau_0 t_n^2\right) \right] \right\}
$$
(A6)

$R_{\text{cross},i,j,6}(f_r, t_n, \tau)$

$$
= 2A_{2i}A_{2j}^3 \exp\left\{ -j4\pi\frac{f_r+f_c}{c}\left[\begin{array}{c} R_{0i} - R_{0j} - (v_i - v_j)t_n + \frac{1}{2}(a_i + 3a_j)\tau\tau_0 + \frac{1}{2}(b_i + 3b_j)\tau\tau_0 t_n \\ - (a_i - a_j)\left(\frac{1}{2}t_n^2 + \frac{1}{8}\tau^2 + \frac{1}{2}\tau_0^2\right) - (b_i - b_j)\left(\frac{1}{6}t_n^3 + \frac{1}{8}\tau^2 t_n + \frac{1}{2}\tau_0^2 t_n\right) \end{array} \right] \right\}
$$

$$
\times \cos\left\{ 4\pi\frac{f_r+f_c}{c}\left[(v_i - v_j)\left(\frac{1}{2}\tau - \tau_0\right) + (a_i - a_j)\left(\frac{1}{2}\tau t_n - \tau_0 t_n\right) + (b_i - b_j)\left(\frac{1}{48}\tau^3 - \frac{1}{6}\tau_0^3 + \frac{1}{4}\tau\tau_0^2 - \frac{1}{8}\tau^2\tau_0 + \frac{1}{4}\tau t_n^2 - \frac{1}{2}\tau_0 t_n^2\right) \right] \right\}
$$
(A7)

The cross-term $Q_{\text{cross},i,j}(t_n, \tau_n)$ in (20) can be expressed as

$$
Q_{\text{cross},i,j}(t_n, \tau_n) = \sum_{p=1}^{6} \text{SUM}_{f_r}\left[Q_{\text{cross},i,j,p}(f_r, t_n, \tau_n) \right]
$$
(A8)

where

$Q_{\text{cross},i,j,1}(f_r, t_n, \tau_n)$

$$
= 2A_{2i}^3 A_{2j} \exp\left\{ j4\pi\frac{f_r+f_c}{c}\left[\begin{array}{c} 3R_{0i} + R_{0j} + (3v_i + v_j)t_n + \frac{1}{2}(a_i - a_j)\frac{f_c\tau_n}{f_r+f_c}\tau_0 + \frac{1}{2}(b_i - b_j)\frac{f_c\tau_n}{f_r+f_c}\tau_0 t_n \\ + (3a_i + a_j)\left(\frac{1}{2}t_n^2 + \frac{1}{8}\left(\frac{f_c\tau_n}{f_r+f_c}\right)^2 + \frac{1}{2}\tau_0^2\right) + (3b_i + b_j)\left(\frac{1}{6}t_n^3 + \frac{1}{8}\left(\frac{f_c\tau_n}{f_r+f_c}\right)^2 t_n + \frac{1}{2}\tau_0^2 t_n\right) \end{array} \right] \right\}
$$

$$
\times \cos\left\{ 4\pi\frac{f_r+f_c}{c}\left[\begin{array}{c} (v_i - v_j)\left(\frac{1}{2}\frac{f_c\tau_n}{f_r+f_c} - \tau_0\right) + (a_i - a_j)\left(\frac{1}{2}\frac{f_c\tau_n}{f_r+f_c}t_n - \tau_0 t_n\right) \\ + (b_i - b_j)\left(\frac{1}{48}\left(\frac{f_c\tau_n}{f_r+f_c}\right)^3 - \frac{1}{6}\tau_0^3 + \frac{1}{4}\frac{f_c\tau_n}{f_r+f_c}\tau_0^2 - \frac{1}{8}\left(\frac{f_c\tau_n}{f_r+f_c}\right)^2\tau_0 + \frac{1}{4}\frac{f_c\tau_n}{f_r+f_c}t_n^2 - \frac{1}{2}\tau_0 t_n^2\right) \end{array} \right] \right\}
$$
(A9)

$Q_{\text{cross},i,j,2}(f_r, t_n, \tau_n)$

$$
= 2A_{2i}^3 A_{2j} \exp\left\{ j4\pi\frac{f_r+f_c}{c}\left[\begin{array}{c} R_{0i} - R_{0j} + (v_i - v_j)t_n - \frac{1}{2}(3a_i + a_j)\frac{f_c\tau_n}{f_r+f_c}\tau_0 - \frac{1}{2}(3b_i + b_j)\frac{f_c\tau_n}{f_r+f_c}\tau_0 t_n \\ + (a_i - a_j)\left(\frac{1}{2}t_n^2 + \frac{1}{8}\left(\frac{f_c\tau_n}{f_r+f_c}\right)^2 - \frac{1}{2}\tau_0^2\right) + (b_i - b_j)\left(\frac{1}{6}t_n^3 + \frac{1}{8}\left(\frac{f_c\tau_n}{f_r+f_c}\right)^2 t_n + \frac{1}{2}\tau_0^2 t_n\right) \end{array} \right] \right\}
$$

$$
\times \cos\left\{ 4\pi\frac{f_r+f_c}{c}\left[\begin{array}{c} (v_i - v_j)\left(\frac{1}{2}\frac{f_c\tau_n}{f_r+f_c} + \tau_0\right) + (a_i - a_j)\left(\frac{1}{2}\frac{f_c\tau_n}{f_r+f_c}t_n + \tau_0 t_n\right) \\ + (b_i - b_j)\left(\frac{1}{48}\left(\frac{f_c\tau_n}{f_r+f_c}\right)^3 + \frac{1}{6}\tau_0^3 + \frac{1}{4}\left(\frac{f_c\tau_n}{f_r+f_c}\right)\tau_0^2 + \frac{1}{8}\left(\frac{f_c\tau_n}{f_r+f_c}\right)^2\tau_0 + \frac{1}{4}\frac{f_c\tau_n}{f_r+f_c}t_n^2 + \frac{1}{2}\tau_0 t_n^2\right) \end{array} \right] \right\}
$$
(A10)

$Q_{\text{cross},i,j,3}(f_r, t_n, \tau_n)$

$$
= 2A_{2i}^2 A_{2j}^2 \exp\left\{ -j4\pi\frac{f_c}{c}\left[\tau_n\tau_0 t_n(b_i + b_j) + \tau_n\tau_0(a_i + a_j) \right] \right\}
$$

$$
\times \cos\left\{ 4\pi\frac{f_r+f_c}{c}\left[2(R_{0i} - R_{0j}) + (a_i - a_j)\left(t_n^2 + \frac{1}{4}\left(\frac{f_c\tau_n}{f_r+f_c}\right)^2 + \tau_0^2\right) + 2(v_i - v_j)t_n + (b_i - b_j)\left(\frac{1}{3}t_n^3 + \frac{1}{4}\left(\frac{f_c\tau_n}{f_r+f_c}\right)^2 t_n + \tau_0^2 t_n\right) \right] \right\}
$$
(A11)

$Q_{\text{cross},i,j,4}(f_r, t_n, \tau_n)$

$$
= 2A_{2i}^2 A_{2j}^2 \exp\left\{ -j4\pi\frac{f_c}{c}\left[2\tau_n\tau_0(a_i + a_j) + 2\tau_n\tau_0 t_n(b_i + b_j) \right] \right\}
$$

$$
\times \cos\left\{ 4\pi\frac{f_r+f_c}{c}\left[\begin{array}{c} (v_i - v_j)\left(\frac{1}{2}\frac{f_c\tau_n}{f_r+f_c} - \tau_0\right) + (a_i - a_j)\left(\frac{1}{2}\frac{f_c\tau_n}{f_r+f_c}t_n - \tau_0 t_n\right) \\ + (b_i - b_j)\left(\frac{1}{48}\left(\frac{f_c\tau_n}{f_r+f_c}\right)^3 - \frac{1}{6}\tau_0^3 + \frac{1}{4}\frac{f_c\tau_n}{f_r+f_c}\tau_0^2 - \frac{1}{8}\left(\frac{f_c\tau_n}{f_r+f_c}\right)^2\tau_0 + \frac{1}{4}\frac{f_c\tau_n}{f_r+f_c}t_n^2 - \frac{1}{2}\tau_0 t_n^2\right) \end{array} \right] \right\}
$$
(A12)

$$Q_{\text{cross},i,j,5}(f_r, t_n, \tau_n)$$

$$= 2A_{2i}A_{2j}^3 \exp\left\{-j4\pi\frac{f_r+f_c}{c}\left[\begin{array}{c} R_{0i} - R_{0j} - (v_i-v_j)t_n + \frac{1}{2}(a_i+3a_j)\frac{f_c\tau_n}{f_r+f_c}\tau_0 + \frac{1}{2}(b_i+3b_j)\frac{f_c\tau_n}{f_r+f_c}\tau_0 t_n \\ + (a_i-a_j)\left(\frac{1}{2}t_n^2 + \frac{1}{8}\left(\frac{f_c\tau_n}{f_r+f_c}\right)^2 + \frac{1}{2}\tau_0^2\right) + (b_i-b_j)\left(\frac{1}{6}t_n^3 + \frac{1}{8}\left(\frac{f_c\tau_n}{f_r+f_c}\right)^2 t_n + \frac{1}{2}\tau_0^2 t_n\right) \end{array}\right]\right\}$$

$$\times \cos\left\{4\pi\frac{f_r+f_c}{c}\left[\begin{array}{c} (v_i-v_j)\left(\frac{1}{2}\frac{f_c\tau_n}{f_r+f_c}+\tau_0\right) + (a_i-a_j)\left(\frac{1}{2}\frac{f_c\tau_n}{f_r+f_c}t_n + \tau_0 t_n\right) \\ + (b_i-b_j)\left(\frac{1}{48}\left(\frac{f_c\tau_n}{f_r+f_c}\right)^3 + \frac{1}{6}\tau_0^3 + \frac{1}{4}\frac{f_c\tau_n}{f_r+f_c}\tau_0^2 + \frac{1}{8}\left(\frac{f_c\tau_n}{f_r+f_c}\right)^2\tau_0 + \frac{1}{4}\frac{f_c\tau_n}{f_r+f_c}t_n^2 + \frac{1}{2}\tau_0 t_n^2\right) \end{array}\right]\right\} \tag{A13}$$

$$Q_{\text{cross},i,j,6}(f_r, t_n, \tau_n)$$

$$= 2A_{2i}A_{2j}^3 \exp\left\{-j4\pi\frac{f_r+f_c}{c}\left[\begin{array}{c} R_{0i} - R_{0j} - (v_i-v_j)t_n + \frac{1}{2}(a_i+3a_j)\frac{f_c\tau_n}{f_r+f_c}\tau_0 + \frac{1}{2}(b_i+3b_j)\frac{f_c\tau_n}{f_r+f_c}\tau_0 t_n \\ - (a_i-a_j)\left(\frac{1}{2}t_n^2 + \frac{1}{8}\left(\frac{f_c\tau_n}{f_r+f_c}\right)^2 + \frac{1}{2}\tau_0^2\right) - (b_i-b_j)\left(\frac{1}{6}t_n^3 + \frac{1}{8}\left(\frac{f_c\tau_n}{f_r+f_c}\right)^2 t_n + \frac{1}{2}\tau_0^2 t_n\right) \end{array}\right]\right\}$$

$$\times \cos\left\{4\pi\frac{f_r+f_c}{c}\left[\begin{array}{c} (v_i-v_j)\left(\frac{1}{2}\frac{f_c\tau_n}{f_r+f_c}-\tau_0\right) + (a_i-a_j)\left(\frac{1}{2}\frac{f_c\tau_n}{f_r+f_c}t_n - \tau_0 t_n\right) \\ + (b_i-b_j)\left(\frac{1}{48}\left(\frac{f_c\tau_n}{f_r+f_c}\right)^3 - \frac{1}{6}\tau_0^3 + \frac{1}{4}\frac{f_c\tau_n}{f_r+f_c}\tau_0^2 - \frac{1}{8}\left(\frac{f_c\tau_n}{f_r+f_c}\right)^2\tau_0 + \frac{1}{4}\frac{f_c\tau_n}{f_r+f_c}t_n^2 - \frac{1}{2}\tau_0 t_n^2\right) \end{array}\right]\right\} \tag{A14}$$

Compared with the self-term in (20), the following three aspects can be observed:

(a) The cosine function terms will degrade the accumulation of the cross-terms. In fact, only when $v_i = v_j$, $a_i = a_j$ and $b_i = b_j$, the cosine function terms equal to 1 [31–34].

(b) After KT, the new coupling between f_r and τ_n is generated, which means the KT does not work for the cross-term.

(c) In contrast to (20), where f_r has been decoupled from τ and t_n, the echo energies will be dispersed by direct summation along f_r.

The cross-term $Q_{\text{cross},i,j}(f_n, f_{\tau_n})$ in (21) can be expressed as

$$Q_{\text{cross},i,j}(f_n, f_{\tau_n}) = \text{FFT}_{\tau_n}\left[\text{SFT}_{t_n}\left[Q_{\text{cross},i,j}(t_n, \tau_n)\right]\right] \tag{A15}$$

It is obvious that the high-order terms related to the time variable τ_n and t_n exist in the cosine terms and the exponential terms in $Q_{\text{cross},i,j}(t_n, \tau_n)$, such as t_n^2, t_n^3, τ_n^2, and τ_n^3. After performing FFT with respect to τ_n and SFT with respect to t_n, all the cross-terms cannot be integrated along straight lines parallel to the t_n axis in the $t_n - f_{\tau_n}$ domain or to the τ_n axis in the $f_n - \tau_n$ domain due to the complex coupling between t_n and τ_n [24]. Therefore, the cross-term $Q_{\text{cross},i,j}(f_n, f_{\tau_n})$ cannot form any peaks in the $f_n - f_{\tau_n}$ domain. Compared with the self-term in (21), the cross terms will be smeared in this transformed domain.

The above analyses show that the cross-terms' contribution cannot be accumulated well, so they are much smaller than those of the self-terms and thus can be ignored.

References

1. Zheng, J.; Liu, H.; Liu, J.; Du, X.; Liu, Q.H. Radar High-Speed Maneuvering Target Detection Based on Three-Dimensional Scaled Transform. *IEEE J. Sel. Top. Appl. Earth Observ. Remote Sens.* **2018**, *11*, 2821–2833. [CrossRef]
2. Zhang, J.; Su, T.; Zheng, J.; He, X. Novel Fast Coherent Detection Algorithm for Radar Maneuvering Target with Jerk Motion. *IEEE J. Sel. Top. Appl. Earth Observ. Remote Sens.* **2017**, *10*, 1792–1803. [CrossRef]
3. Li, X.; Huang, L.; Zhang, S.; Wang, W. Phase Compensation and Time-Reversal Transform for High-Order Maneuvering Target Detection. *IEEE Geosci. Remote Sens. Lett.* **2022**, *19*, 1–5. [CrossRef]
4. You, P.; Ding, Z.; Liu, S.; Zhang, G. Dechirp-receiving Radar Target Detection Based on Generalized Radon-Fourier Transform. *IET Radar Sonar Navig.* **2021**, *15*, 1096–1111. [CrossRef]
5. Jin, K.; Lai, T.; Wang, Y.; Li, G.; Zhao, Y. Coherent Integration for Radar High-Speed Maneuvering Target Based on Frequency-Domain Second-Order Phase Difference. *Electronics* **2019**, *8*, 287. [CrossRef]
6. Gao, X.; Zhang, H.; Dang, T. Radar Detection and Fast Motion Parameter Estimation for Complex Manoeuvering Targets at High Speed and Acceleration. *IET Radar Sonar Navig.* **2022**, *16*, 1977–1996. [CrossRef]
7. Wan, J.; He, Z.; Tan, X.; Li, D.; Liu, H.; Shu, Y.; Chen, Z. Coherent Integration for Maneuvering Target Detection via Fast Nonparametric Estimation Method. *Signal Process.* **2023**, *203*, 108820. [CrossRef]
8. Zhang, Z.; Liu, N.; Hou, Y.; Zhang, S.; Zhang, L. A Coherent Integration Segment Searching Based GRT-GRFT Hybrid Integration Method for Arbitrary Fluctuating Target. *Remote Sens.* **2022**, *14*, 2695. [CrossRef]

9. Yao, D.; Zhang, X.; Sun, Z. Long-Time Coherent Integration for Maneuvering Target Based on Second-Order Keystone Transform and Lv's Distribution. *Electronics* **2022**, *11*, 1961. [CrossRef]

10. Zhu, D.Y.; Li, Y.; Zhu, Z.D. A Keystone Transform Without Interpolation for SAR Ground Moving-Target Imaging. *IEEE Geosci. Remote Sens. Lett.* **2007**, *4*, 18–22. [CrossRef]

11. Su, J.; Xing, M.; Wang, G.; Bao, Z. High-Speed Multi-Target Detection with Narrowband Radar. *IET Radar Sonar Navig.* **2010**, *4*, 595. [CrossRef]

12. Rao, X.; Tao, H.; Su, J.; Guo, X.; Zhang, J. Axis Rotation MTD Algorithm for Weak Target Detection. *Digit. Signal Prog.* **2014**, *26*, 81–86. [CrossRef]

13. Zheng, J.; Su, T.; Zhu, W.; He, X.; Liu, Q.H. Radar High-Speed Target Detection Based on the Scaled Inverse Fourier Transform. *IEEE J. Sel. Top. Appl. Earth Observ. Remote Sens.* **2015**, *8*, 1108–1119. [CrossRef]

14. Chen, X.; Guan, J.; Liu, N.; He, Y. Maneuvering Target Detection via Radon-Fractional Fourier Transform-Based Long-Time Coherent Integration. *IEEE Trans. Signal Process.* **2014**, *62*, 939–953. [CrossRef]

15. Li, X.; Sun, Z.; Yi, W.; Cui, G.; Kong, L.; Yang, X.B. Computationally Efficient Coherent Detection and Parameter Estimation Algorithm for Maneuvering Target. *Signal Process.* **2019**, *155*, 130–142. [CrossRef]

16. Li, X.; Cui, G.; Yi, W.; Kong, L. Manoeuvring Target Detection Based on Keystone Transform and Lv's Distribution. *IET Radar Sonar Navig.* **2016**, *10*, 1234–1242. [CrossRef]

17. Pang, C.; Liu, S.; Han, Y. Coherent Detection Algorithm for Radar Maneuvering Targets Based on Discrete Polynomial-Phase Transform. *IEEE J. Sel. Top. Appl. Earth Observ. Remote Sens.* **2019**, *12*, 3412–3422. [CrossRef]

18. Xu, J.; Xia, X.G.; Peng, S.B.; Ji, Y.; Peng, Y.N.; Qian, L.C. Radar Maneuvering Target Motion Estimation Based on Generalized Radon-Fourier Transform. *IEEE Trans. Signal Process.* **2012**, *60*, 6190–6201. [CrossRef]

19. Li, X.; Cui, G.; Kong, L.; Yi, W. Fast Non-Searching Method for Maneuvering Target Detection and Motion Parameters Estimation. *IEEE Trans. Signal Process.* **2016**, *64*, 2232–2244. [CrossRef]

20. Zheng, J.; Su, T.; Liu, H.; Liao, G.; Liu, Z.; Liu, Q. Radar High-Speed Target Detection Based on the Frequency-Domain Deramp-Keystone Transform. *IEEE J. Sel. Top. Appl. Earth Observ. Remote Sens.* **2016**, *9*, 285–294. [CrossRef]

21. Bai, X.; Tao, R.; Wang, Z.; Wang, Y. ISAR Imaging of a Ship Target Based on Parameter Estimation of Multicomponent Quadratic Frequency-Modulated Signals. *IEEE Trans. Geosci. Remote Sens.* **2014**, *52*, 1418–1429. [CrossRef]

22. Cao, R.; Li, M.; Zuo, L.; Sun, H. Fast Parameter Estimation Method for Maneuvering Target by Using Non-Uniformly Resampling Reducing Order Technique. *Signal Process.* **2019**, *160*, 299–315. [CrossRef]

23. Djurovic, I.; Simeunovic, M.; Djukanovic, S.; Wang, P. A Hybrid CPF-HAF Estimation of Polynomial-Phase Signals: Detailed Statistical Analysis. *IEEE Trans. Signal Process.* **2012**, *60*, 5010–5023. [CrossRef]

24. Huang, P.; Xia, X.; Liao, G.; Yang, Z.; Zhou, J.; Liu, X. Ground Moving Target Refocusing in SAR Imagery Using Scaled GHAF. *IEEE Trans. Geosci. Remote Sens.* **2018**, *56*, 1030–1045. [CrossRef]

25. Li, X.; Kong, L.; Cui, G.; Yi, W. CLEAN-based Coherent Integration Method for High-speed Multi-targets Detection. *IET Radar Sonar Navig.* **2016**, *10*, 1671–1682. [CrossRef]

26. Li, Y.; Zhang, J.; Niu, J.; Zhou, Y.; Wang, L. Computational Implementation and Asymptotic Statistical Performance Analysis of Range Frequency Autocorrelation Function for Radar High-Speed Target Detection. *IEEE Trans. Comput. Imaging* **2020**, *6*, 1297–1308. [CrossRef]

27. Barbarossa, S. Analysis of Multicomponent LFM Signals by a Combined Wigner-Hough Transform. *IEEE Trans. Signal Process.* **1995**, *43*, 1511–1515. [CrossRef]

28. Li, Y.; Zhang, J.; Zheng, J.; Niu, J.; Zhou, Y.; Meng, N. ISAR Imaging of Nonuniformly Rotating Targets With Low SNR Based on Third Order Autocorrelation Function. *IEEE Access.* **2020**, *8*, 74707–74719. [CrossRef]

29. Barton, D.K. *Radar System Analysis and Modeling*; Artech House: Norfolk County, MA, USA, 2004; ISBN 1-58053-681-6.

30. Song, Z.; Hui, B.; Fan, H.; Zhou, J.; Zhu, Y.; Da, K.; Zhang, X.; Su, H.; Jin, W.; Zhang, Y. A dataset for dim target detection and tracking of aircraft in radar echo sequences. *Sci. Data Bank* **2019**. [CrossRef]

31. Zhang, J.; Li, Y.; Su, T.; He, X. Quadratic FM Signal Detection and Parameter Estimation Using Coherently Integrated Trilinear Autocorrelation Function. *IEEE Trans. Signal Process.* **2020**, *68*, 621–633. [CrossRef]

32. Li, D.; Zhan, M.; Su, J.; Liu, H.; Zhang, X.; Liao, G. Performances Analysis of Coherently Integrated CPF for LFM Signal Under Low SNR and Its Application to Ground Moving Target Imaging. *IEEE Trans. Geosci. Remote Sens.* **2017**, *55*, 6402–6419. [CrossRef]

33. Gao, X.; Zhang, H. Radar Coherent Integration Algorithm for Detection of Complexly Maneuvering Target with Extended Velocity and Acceleration Scopes. *Digit. Signal Process.* **2022**, *129*, 103689. [CrossRef]

34. Huang, P.; Liao, G.; Yang, Z.; Xia, X.-G.; Ma, J.; Zheng, J. Ground Maneuvering Target Imaging and High-Order Motion Parameter Estimation Based on Second-Order Keystone and Generalized Hough-HAF Transform. *IEEE Trans. Geosci. Remote Sens.* **2017**, *55*, 320–335. [CrossRef]